6-24-2019

Feasibility of generating synthetic CT from T1-weighted MRI using a linear mixed-effects regression model

Anant Pandey
Louisiana State University

S. A. Yoganathan
Louisiana State University

Beibei Guo
Louisiana State University

Rui Zhang
Louisiana State University

Recommended Citation

Pandey, A., Yoganathan, S., Guo, B., & Zhang, R. (2019). Feasibility of generating synthetic CT from T1-weighted MRI using a linear mixed-effects regression model. *Biomedical Physics and Engineering Express, 5* (4) https://doi.org/10.1088/2057-1976/ab27a6

HHS Public Access

Author manuscript

Biomed Phys Eng Express. Author manuscript; available in PMC 2020 July 01.

Published in final edited form as:

Biomed Phys Eng Express. 2019 July ; 5(4): . doi:10.1088/2057-1976/ab27a6.

Feasibility of generating synthetic CT from T1-weighted MRI using a linear mixed-effects regression model

Anant Pandey[1,2], **Yoganathan SA**[1], **Beibei Guo**[3], **Rui Zhang**[1,4,5]

[1]Department of Physics & Astronomy, Louisiana State University, Baton Rouge, Louisiana, USA

[2]Department of Physics, Sri Venkateswara College, University of Delhi, Benito Juarez Road, New Delhi, India

[3]Department of Experimental Statistics, Louisiana State University, Baton Rouge, Louisiana, USA

[4]Department of Radiation Oncology, Mary Bird Perkins Cancer Center, 4950 Essen Lane, Baton Rouge, Louisiana, USA

Abstract

Generation of synthetic computed tomography (sCT) for magnetic resonance imaging (MRI)-only radiotherapy is emerging as a promising direction because it can eliminate the registration error and simplify clinical workflow. The goal of this study was to generate accurate sCT from standard T1-weighted MRI for brain patients. CT and MRI data of twelve patients with brain tumors were retrospectively collected. Linear mixed-effects (LME) regression models were fitted between CT and T1-weighted MRI intensities for different segments in the brain. The whole brain sCTs were generated by combining predicted segments together. Mean absolute error (MAE) between real CTs and sCTs across all patients was 71.1 ± 5.5 Hounsfield Unit (HU). Average differences in the HU values were 1.7 ± 7.1 HU (GM), 0.9 ± 5.1 HU (WM), −24.7 ± 8.0 HU (CSF), 76.4 ± 17.8 HU (bone), 20.9 ± 20.4 HU (fat), −69.4 ± 28.3 HU (air). A simple regression technique has been devised that is capable of producing accurate HU maps from standard T1-weighted MRI, and exceptionally low MAE values indicate accurate prediction of sCTs. Improvement is needed in segmenting MRI using a more automatic approach.

Keywords

synthetic CT; MRI; linear mixed-effects regression; radiotherapy

1. Introduction

Magnetic resonance imaging (MRI) gives better anatomical and functional information compared to computed tomography (CT) when dealing with soft tissues, which helps in accurate differentiation of tumor from surrounding organs at risk (OAR) during radiotherapy treatment planning (RTP) (Mitchell *et al.*, 2006; Devic, 2012). However, CT remains the fundamental standard imaging modality for RTP mainly because of the direct relationship

[5]Author to whom any correspondence should be addressed: rzhang@lsu.edu.

between CT Hounsfield Unit (HU) value and electron density that is exploited for dose calculations, while such a direct relationship is non-existent for MRI. CT also provides an accurate bony anatomy which is necessary for generating digitally reconstructed radiographs (DRRs) for patient positioning verification. Using the two imaging modalities together, which requires bringing of soft tissue structure contours of MRI images onto the CT scans, has its own advantages (Villeirs *et al.*, 2005; Devic, 2012), but may result in systematic errors which are inherent in the process of MRI-to-CT co-registration (Roberson *et al.*, 2005). These systematic errors can potentially result in an increased dose to OAR and a substantial miss of the target volume. Moreover, the MRI-CT workflow introduces additional ionizing radiation exposure to the patient and puts extra financial and infrastructural burden on the health care system.

Lately, interest among researchers has developed in completely replacing CT with MRI (Edmund and Nyholm, 2017; Johnstone *et al.*, 2018), which will not only eliminate the co-registration errors but also reduce the number of scanning sessions for the patient. Broadly speaking, five types of techniques have been used to generate synthetic CT (sCT) namely the bulk density assignment, the atlas-based, the voxel-based, the hybrid, and the deep learning techniques. The bulk density assignment technique is based on assigning bulk electron densities to different tissue segments separated manually or automatically from an MRI image (Lee *et al.*, 2003; Eilertsen *et al.*, 2008), which may introduce unacceptable dose error and cannot generate accurate DRRs (mainly based on bony structures) for patient positioning verification. The atlas-based methods largely depend on deformable registration of CT/MRI atlas pairs on the MRI image of a new patient (Dowling *et al.*, 2012; Demol *et al.*, 2016). Such methods have inherent registration uncertainties due to inter-patient anatomical differences. The voxel-based methods aim to characterize tissue properties based on MRI voxel intensities (Johansson *et al.*, 2011; Hsu *et al.*, 2013; Korhonen *et al.*, 2014). However, these methods often generate ambiguous results because of the absence of a direct one-to-one correspondence between MRI voxel intensity and electron density. Moreover, lack of difference between bone and air in the conventional MRI sequences also complicates the matter further. Some groups have used unconventional MRI sequences like the ultra-short echo time (UTE) to overcome this problem (Johansson *et al.*, 2011). However, image quality of UTE sequence has been reported to be far from satisfactory as blood vessels and bone may appear indistinguishable in such images (Hsu *et al.*, 2013), and this unconventional MRI sequence adds significant scan time thus increasing the possibility of patient movement and discomfort. The hybrid methods that combine atlas-based and voxel-based methods can still be over reliant on a single or multiple image registrations and only improve the accuracy of sCT moderately (Gudur *et al.*, 2014). Approaches using deep learning have shown great promise recently (Han, 2017; Emami *et al.*, 2018; Xiang *et al.*, 2018). However, training of the neural network model itself takes a couple of days even though it needs to be done only once, and mean absolute error (MAE) between sCT and real CT is still over 80 HU for brain tumor patients.

In the present work, a voxel-based linear mixed-effects (LME) regression model is being reported and it has been found to be effective in generating an accurate sCT from a patient's conventional T-1 weighted MRI image of the brain. The sCTs were compared geometrically with their corresponding real CTs.

2. Materials and methods

2.1 Image acquisition and processing

Whole head MRI and CT scans were obtained from twelve patients in our institution and were anonymized for this research (Newhauser *et al.*, 2014). The criteria of selection are: patients undergo radiotherapy for brain tumors in our institution with both CT and MRI available; both CT and MR should be free of motion artifacts; CT and MR should be acquired on the same day to exclude any anatomical variation. These patients were randomly selected from a collection of patients having undergone stereotactic radiosurgery in our institute within last 10 years, and should represent the whole brain patient population. Standard T1-weighted MRI images were obtained from 1.5 Tesla Phillips Intera scanner using 3D GRE sequence with TE/TR= 3.414/7.33 ms, flip angle = 8º, voxel size 0.9833 × 0.9833 × 1.1 mm^3, field of view (FOV) 236 × 236 × 158.4 mm^3 and pixel bandwidth 241 Hz/pixel. CT images were acquired from GE LightSpeed RT 16 CT scanner operating at 140 kVp and 380 mAs with voxel resolution 0.703125 × 0.703125 × 1.25 mm^3 and FOV 360 × 360 × 190 mm^3.

An open source software 3D Slicer (version 4.8) was used for image processing. All the MRI and CT images were re-sampled to voxel sizes 1×1×1 mm^3 for uniformity and all non-tissue, background voxels outside the brain were removed through segmentation editor in 3D-Slicer. MRI bias correction was also applied using the N4itk MRI Bias correction module available in 3D-slicer. The MRI-CT image pair of each patient was then co-registered using affine registration. A single patient was selected randomly as reference and all the remaining patients' MRI and CT images were registered with reference patients' MRI and CT images using affine method in 3D Slicer. Using a combination of volumetric segmentation based on density threshold in 3D Slicer and automatic segmentation in another open source software volBrain (Manjon and Coupe, 2016), six different regions namely gray matter (GM), white matter (WM), fat, cerebrospinal fluid (CSF), air and bone in the CT and MRI images of all patients were segmented: bone and air regions were segmented on CT images using density threshold option in 3D Slicer while GM, WM and CSF were segmented on MRI images using volBrain; because each patient's MRI and CT images were co-registered, the segmentations on one image can be copied over to the other and the remaining parts that were not segmented on either side will be segmented as fat using morphological operations; to obtain better HU mapping, bone was further divided into low- (<800 HU), medium- (800 ~1200 HU) and high-density (>1200 HU) bones.

2.2 sCT generation

MATLAB (Mathworks, Natick, MA) programming was used for fitting an LME regression model between a segment's CT HU values and the corresponding MR intensities with their spatial indices (x, y, z) of voxels. Each patient was assigned a numerical number starting from 1 for patient one to 12 for patient twelve, and this patient number was used for the random effect on the intercept as shown by equation (1):

$$CT = K[1 + MRI + X + Y + Z + (1|PatientNumber)] \quad (1)$$

where *MRI*, *X*, *Y*, and *Z* are the predictor variables, *PatientNumber* is being used for the random effect, and *K* is a matrix of coefficients obtained from the derived LME model. Similar models were fitted for all eight different segments (GM, WM, CSF, fat, air, low-density bone, medium-density bone and high-density bone). It is to be noted here that for all three bone segments, reciprocal values of the MRI intensities were used for the *MRI* variable so as to establish an inversely proportional relationship between HU values and MR intensities (Yu *et al.*, 2014). The function *fitlme* from MATLAB was used with the following parameters: CovariancePattern: FullCholesky, FitMethod: Maximum likelihood estimation, Maximum number of iterations allowed: 10000. Performance of the LME model was evaluated using leave-one-out cross validation (LOOCV) approach: LME models were fitted based on the data of any eleven patients (training) and these models were used to predict the segments for the remaining twelfth patient (validation) in the study dataset, and this procedure is repeated for all possible combinations of training and validation data. The eight different segments (with their HU maps) thus predicted for a patient were then simply combined together to generate the sCT of that patient. Figure 1 shows a schematic of sCT generation.

2.3 Image evaluation

Differences in HU values between sCT and real CT of each patient for the six different segments (with a combination of low-, medium- and high-density bones taken as a single segment) as well as the full FOV (within the head region) were analyzed. MAE was calculated using equation (2):

$$MAE = \frac{\sum_{i=1}^{N} |(CT(i) - sCT(i))|}{N} \quad (2)$$

where *N* is the total number of image voxels, *i* corresponds to the voxel number in CT or sCT.

3. Results

Figure 2 (a) shows axial views of CT and MRI scans of a typical patient in this study along with the binary mask images corresponding to the six different segments, and the three sub-segments of bone are shown separately in figure 2 (b). Figure 3 shows the real CT and sCT of a typical patient (number 12) along with the difference map. It can be seen that over- and under-predictions are prominent at air-tissue or bone-tissue interface regions, which is consistent with the literature (Johansson *et al.*, 2012; Andreasen *et al.*, 2015). On a workstation with a dual 2.6 GHz Intel Xenon E5–2670 processor and 64 GB Intel RAM, LME model training (required only once) takes around 50 minutes, image segmentations take less than 3 minutes for each patient, and sCT prediction takes 4–5 minutes for each patient. Table 1 shows the MAE values for all the patients and the average MAE was 71.1 ± 5.5 HU within patients' head region. The main reason for the highest MAE value for patient 10 is the metal artifacts caused by dental filling materials. As shown in figure 4, the CT for patient 10 shows streak artifacts while the MRI on the same slice shows void signal

in the same area. The artifacts create uncertainties in tissue segmentation and HU value prediction. Differences in the average HU values of the six segments between real CT and sCT of all twelve patients were: 1.7 ± 7.1 HU (GM), 0.9 ± 5.1 HU (WM), −24.7 ± 8.0 HU (CSF), 76.4 ± 17.8 HU (bone), 20.9 ± 20.4 HU (fat), −69.4 ± 28.3 HU (air). Table 2 compares our study with previous sCT studies using brain tumor patients.

4. Discussion

A LME regression method was developed to generate sCT for MRI-only RTP. Compared with previous studies, our research is innovative: (1) it utilizes a novel and simple LME model which consists of both conventional linear regression and the random effects. The model is much simpler than the Bayesian framework used in the literature (Gudur *et al.*, 2014) and superior to other statistical models that do not integrate intensity and geometry information (Johansson *et al.*, 2011; Hsu *et al.*, 2013); (2) it only needs standard T1-weighted MRI, which makes our methods easy to implement and avoids the issues associated with specialized sequences; (3) it does not require deformable registration between training and new patients like previous studies (Dowling *et al.*, 2012; Gudur *et al.*, 2014; Uh *et al.*, 2014; Demol *et al.*, 2016), which avoids the possible uncertainties or errors associated with deformable image registration.

Even though radiological and dosimetric evaluations still need to be completed, excellent HU value agreement between real CT and sCT as found in the geometric evaluation suggests that our method has a good potential for MRI-only RTP workflow. The MAE value observed with this method was lower than those obtained by others ranging between 80 HU to 200 HU for the brain as shown in Table 2. Moreover, some of the techniques in other studies were much more complex than our method. A major limitation of the present method of generating sCT is its dependence on a semi-automatic segmentation of MRI which relies on the availability of CT images for bone and air segmentation, while CT images will not be available for a new patient in MRI-only RTP. We are working towards making the segmentation process completely automatic and removing any dependence on the availability of CT images. It is anticipated that an exhaustive work using the present LME regression technique along with automatic segmentation based on MRI only and radiological and dosimetric assessment of sCTs will be shortly communicated as a full-length paper.

5. Conclusions

Using a LME model, accurate relationships have been established between CT HU values and MRI intensities for different segments within the brain. This should be exploited to generate reliable sCT for MRI-only RTP.

Acknowledgements

This work was partially supported by National Institutes of Health (grant no. K22CA204464).

References

Andreasen D, Van Leemput K, Hansen RH, Andersen JA and Edmund JM 2015 Patch-based generation of a pseudo CT from conventional MRI sequences for MRI-only radiotherapy of the brain Med Phys 42 1596–605 [PubMed: 25832050]

Demol B, Boydev C, Korhonen J and Reynaert N 2016 Dosimetric characterization of MRI-only treatment planning for brain tumors in atlas-based pseudo-CT images generated from standard T1-weighted MR images Med Phys 43 6557 [PubMed: 27908187]

Devic S 2012 MRI simulation for radiotherapy treatment planning Med Phys 39 6701–11 [PubMed: 23127064]

Dowling JA, Lambert J, Parker J, Salvado O, Fripp J, Capp A, Wratten C, Denham JW and Greer PB 2012 An atlas-based electron density mapping method for magnetic resonance imaging (MRI)-alone treatment planning and adaptive MRI-based prostate radiation therapy Int J Radiat Oncol Biol Phys 83 e5–11 [PubMed: 22330995]

Edmund JM and Nyholm T 2017 A review of substitute CT generation for MRI-only radiation therapy Radiat Oncol 12 28 [PubMed: 28126030]

Eilertsen K, Vestad LN, Geier O and Skretting A 2008 A simulation of MRI based dose calculations on the basis of radiotherapy planning CT images Acta Oncol 47 1294–302 [PubMed: 18663645]

Emami H, Dong M, Nejad-Davarani SP and Glide-Hurst CK 2018 Generating synthetic CTs from magnetic resonance images using generative adversarial networks Med Phys

Gudur MS, Hara W, Le QT, Wang L, Xing L and Li R 2014 A unifying probabilistic Bayesian approach to derive electron density from MRI for radiation therapy treatment planning Phys Med Biol 59 6595–606 [PubMed: 25321341]

Han X 2017 MR-based synthetic CT generation using a deep convolutional neural network method Med Phys 44 1408–19 [PubMed: 28192624]

Hsu SH, Cao Y, Huang K, Feng M and Balter JM 2013 Investigation of a method for generating synthetic CT models from MRI scans of the head and neck for radiation therapy Phys Med Biol 58 8419–35 [PubMed: 24217183]

Johansson A, Karlsson M and Nyholm T 2011 CT substitute derived from MRI sequences with ultrashort echo time Med Phys 38 2708–14 [PubMed: 21776807]

Johansson A, Karlsson M, Yu J, Asklund T and Nyholm T 2012 Voxel-wise uncertainty in CT substitute derived from MRI Med Phys 39 3283–90 [PubMed: 22755711]

Johnstone E, Wyatt JJ, Henry AM, Short SC, Sebag-Montefiore D, Murray L, Kelly CG, McCallum HM and Speight R 2018 Systematic Review of Synthetic Computed Tomography Generation Methodologies for Use in Magnetic Resonance Imaging-Only Radiation Therapy Int J Radiat Oncol Biol Phys 100 199–217 [PubMed: 29254773]

Koivula L, Wee L and Korhonen J 2016 Feasibility of MRI-only treatment planning for proton therapy in brain and prostate cancers: Dose calculation accuracy in substitute CT images Med Phys 43 4634 [PubMed: 27487880]

Korhonen J, Kapanen M, Keyrilainen J, Seppala T and Tenhunen M 2014 A dual model HU conversion from MRI intensity values within and outside of bone segment for MRI-based radiotherapy treatment planning of prostate cancer Med Phys 41 011704 [PubMed: 24387496]

Lee YK, Bollet M, Charles-Edwards G, Flower MA, Leach MO, McNair H, Moore E, Rowbottom C and Webb S 2003 Radiotherapy treatment planning of prostate cancer using magnetic resonance imaging alone Radiother Oncol 66 203–16 [PubMed: 12648793]

Manjon JV and Coupe P 2016 volBrain: An Online MRI Brain Volumetry System Frontiers in neuroinformatics 10 30 [PubMed: 27512372]

Mitchell DG, Snyder B, Coakley F, Reinhold C, Thomas G, Amendola M, Schwartz LH, Woodward P, Pannu H and Hricak H 2006 Early invasive cervical cancer: tumor delineation by magnetic resonance imaging, computed tomography, and clinical examination, verified by pathologic results, in the ACRIN 6651/GOG 183 Intergroup Study J Clin Oncol 24 5687–94 [PubMed: 17179104]

Newhauser WD, Jones T, Swerdloff S, Newhauser W, Cilia M, Carver R, Halloran A and Zhang R 2014 Anonymization of DICOM electronic medical records for radiation therapy Computers in biology and medicine 53 134–40 [PubMed: 25147130]

Price RG, Kim JP, Zheng W, Chetty IJ and Glide-Hurst C 2016 Image Guided Radiation Therapy Using Synthetic Computed Tomography Images in Brain Cancer Int J Radiat Oncol Biol Phys 95 1281–9 [PubMed: 27209500]

Rank CM, Hunemohr N, Nagel AM, Rothke MC, Jakel O and Greilich S 2013 MRI-based simulation of treatment plans for ion radiotherapy in the brain region Radiother Oncol 109 414–8 [PubMed: 24268939]

Roberson PL, McLaughlin PW, Narayana V, Troyer S, Hixson GV and Kessler ML 2005 Use and uncertainties of mutual information for computed tomography/ magnetic resonance (CT/MR) registration post permanent implant of the prostate Med Phys 32 473–82 [PubMed: 15789594]

Su KH, Hu L, Stehning C, Helle M, Qian P, Thompson CL, Pereira GC, Jordan DW, Herrmann KA, Traughber M, Muzic RF Jr. and Traughber BJ 2015 Generation of brain pseudo-CTs using an undersampled, single-acquisition UTE-mDixon pulse sequence and unsupervised clustering Med Phys 42 4974–86 [PubMed: 26233223]

Uh J, Merchant TE, Li Y, Li X and Hua C 2014 MRI-based treatment planning with pseudo CT generated through atlas registration Med Phys 41 051711 [PubMed: 24784377]

Villeirs GM, Van Vaerenbergh K, Vakaet L, Bral S, Claus F, De Neve WJ, Verstraete KL and De Meerleer GO 2005 Interobserver delineation variation using CT versus combined CT + MRI in intensity-modulated radiotherapy for prostate cancer Strahlenther Onkol 181 424–30 [PubMed: 15995835]

Xiang L, Wang Q, Nie D, Zhang L, Jin X, Qiao Y and Shen D 2018 Deep embedding convolutional neural network for synthesizing CT image from T1-Weighted MR image Medical image analysis 47 31–44 [PubMed: 29674235]

Yu H, Caldwell C, Balogh J and Mah K 2014 Toward magnetic resonance-only simulation: segmentation of bone in MR for radiation therapy verification of the head Int J Radiat Oncol Biol Phys 89 649–57 [PubMed: 24803040]

Zheng W, Kim JP, Kadbi M, Movsas B, Chetty IJ and Glide-Hurst CK 2015 Magnetic Resonance-Based Automatic Air Segmentation for Generation of Synthetic Computed Tomography Scans in the Head Region Int J Radiat Oncol Biol Phys 93 497–506 [PubMed: 26460991]

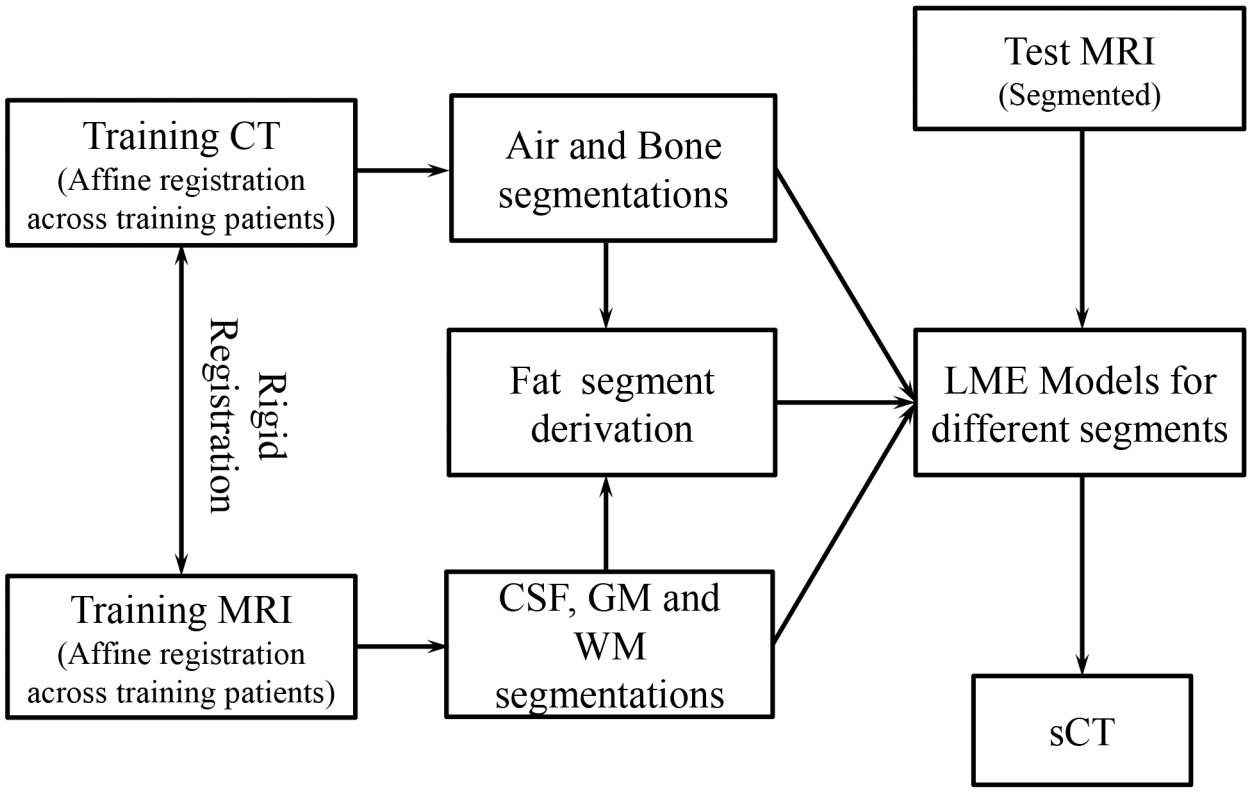

Figure 1.
A schematic of the sCT generation procedure used in this work.

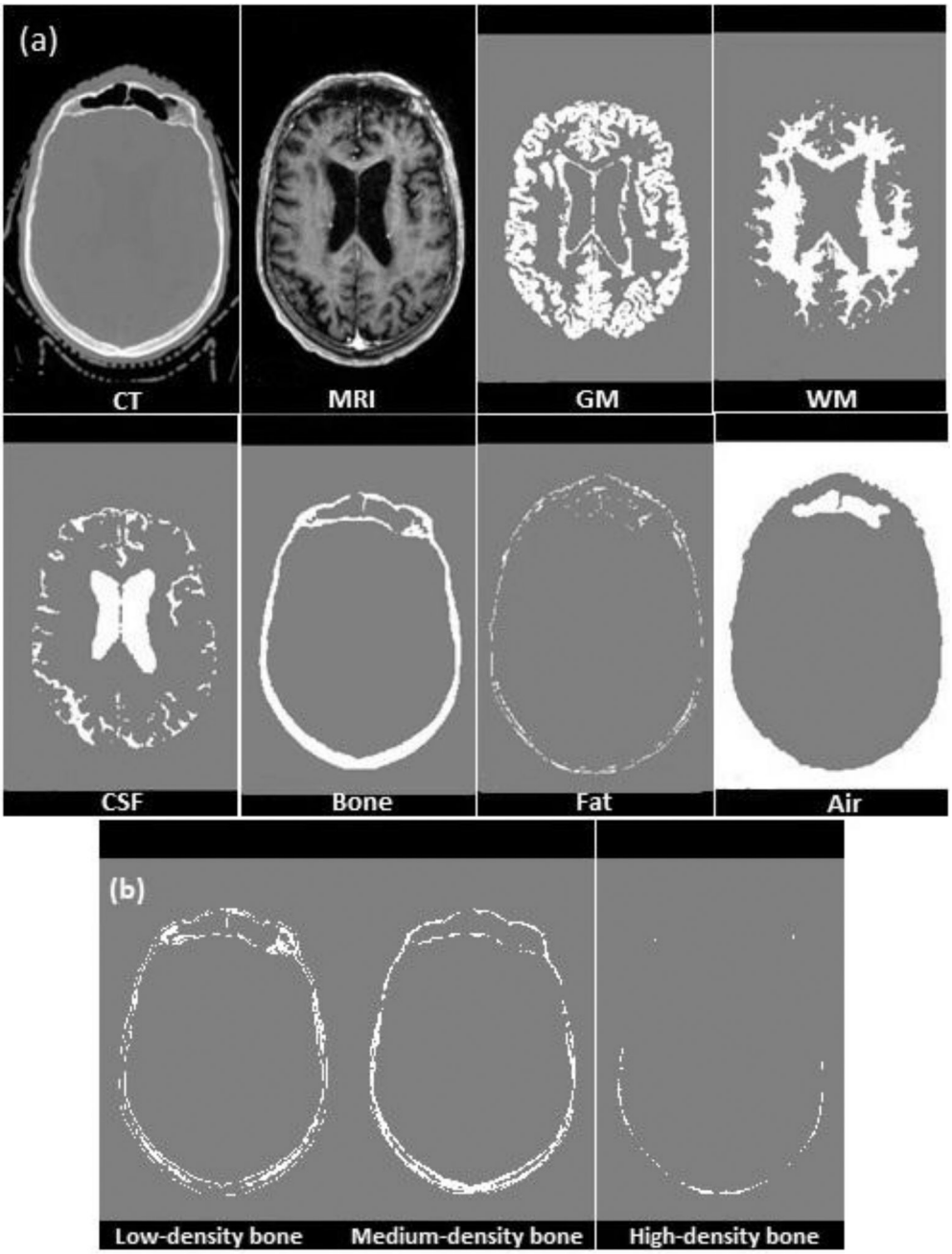

Figure 2.
(a) Axial views of CT, MRI, segmentations of GM, WM, CSF, bone, fat, and air on the same slice for a typical patient in this study. (b) Axial view of bone segment which is further subdivided into low-, medium- and high-density bones.

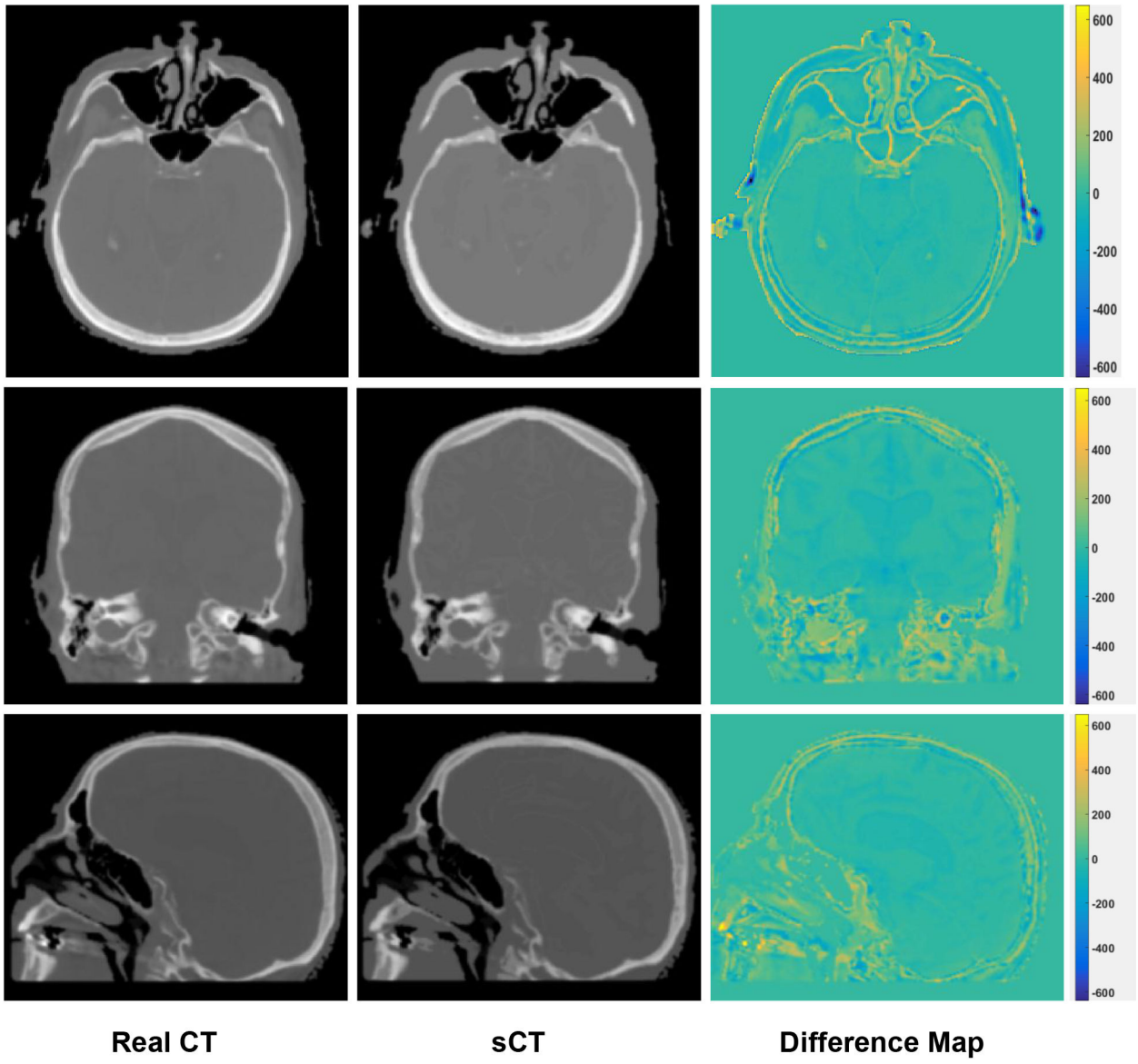

Figure 3.

Axial (first row), coronal (second row) and sagittal (third row) slices of real CT, sCT, and their difference map for a typical patient (number 12).

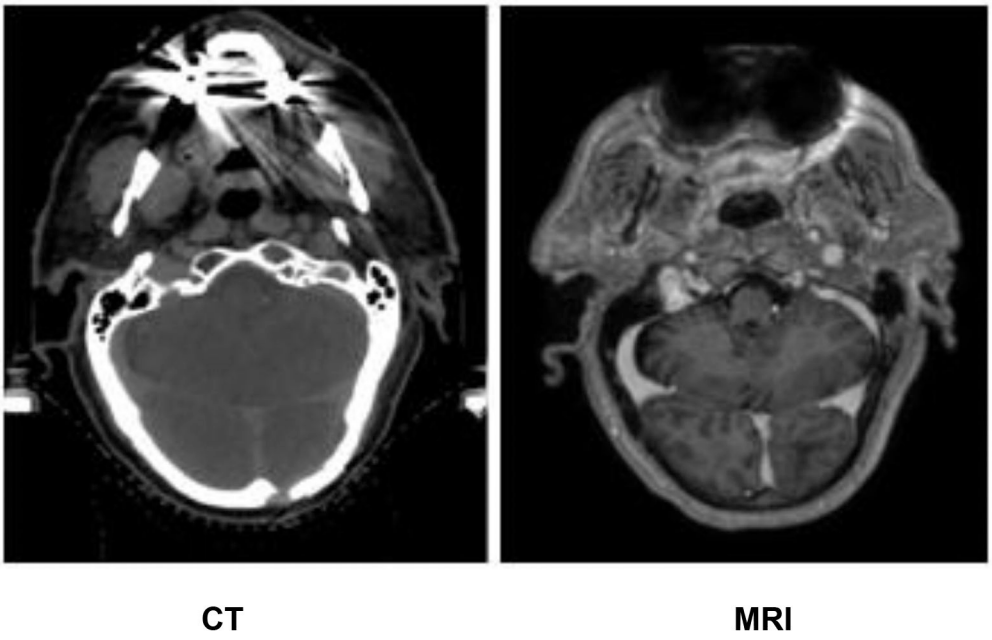

Figure 4.
CT and MRI images for patient 10.

Table 1.

The individual MAE (HU) values for all 12 patients, the mean MAE and standard deviation (STD).

	Patient number													
	1	**2**	**3**	**4**	**5**	**6**	**7**	**8**	**9**	**10**	**11**	**12**	**Mean**	**STD**
MAE	68.0	70.9	66.4	76.7	69.9	69.5	74.7	66.5	72.4	80.4	60.7	76.6	71.1	5.5

Table 2.

Comparison with previous sCT studies using brain tumor patients.

Authors	Technique used to generate sCT	Num of patients	Computation time	Mean difference between sCT and real CT (HU)
Johansson *et al.*, (2011)	Voxel-based, UTE and T2-weighted SPACE MRI sequences	5	Model training time N/A. 110 s for sCT generation	137 mean MAE (for voxels inside the binary mask)
Rank *et al.*, (2013)	Voxel-based, TSE, UTE MRI sequences	3	N/A	140.7~165.2 MAE (for masked voxels)
Uh *et al.*, (2014)	Atlas-based, standard T2-weighted MRI	26	271.4 minutes for the best method	207 ± 33 root mean square difference (for the best method)
Gudur *et al.*, (2014)	Hybrid technique, standard T1-weighted MRI	9	N/A	126 ± 25 MAE (within the head region)
Zheng *et al.*, (2015)	Voxel-based, UTE/Dixon, T1-FFE, T2-TSE, FLAIR MRI	10	N/A	147.5 ± 8.3 MAE (for full FOV)
Su *et al.*, (2015)	Voxel-based, unsupervised clustering, UTE MRI	9	Average clustering time per patient is 67.3 s for FCM_{COMKAT} and 123.1 s for $FCM_{toolbox}$	130±16 mean absolute prediction deviation (for the entire volume)
Andreasen *et al.*, (2015)	Atlas-based (patch) method, standard T1-weighted MRI	5	15 hours	85 ± 14 MAE (within the head region)
Price *et al.*, (2016)	Voxel-based, UTE/Dixon, T1-FFE, T2-TSE, FLAIR MRI	12	N/A	149.2 ± 8.7 MAE (for full FOV)
Koivula *et al.*, (2016)	Voxel-based, intensity-based dual model, standard MRI sequences	10	Conversion time from MRI to sCT 30 s per patient	34 MAE (excluding air cavities in the head. Not comparable with other studies)
Han *et al.*, (2017)	Deep learning convolutional neural network, standard T1-weighted MRI	18	2.5 days for model training, 9 s for sCT generation	84.8 ± 17.3 MAE (within the head region)
Emami *et al.*, (2018)	Deep learning generative adversarial networks, standard T1-weighted MRI	15	11 hours for GAN training, 5.7 ± 0.6 s for sCT generation	89.3 ± 10.3 MAE (within the head region)
Xiang *et al.*, (2018)	Deep learning embedding convolutional neural network, standard T1-weighted MRI	16	2–3 days for model training, 46 s for sCT generation	85.4 ± 9.24 MAE (within the head region)
Our study	Voxel-based, LME regression model, standard T1-weighted MRI	12	50 minutes for model training, 3 minutes for segmentation, 4–5 minutes for sCT generation	71.1 ± 5.5 MAE (within the head region)